

Nanoscale Advances

Accepted Manuscript

This article can be cited before page numbers have been issued, to do this please use: A. Raza, P. Noh, Y. Jaehyeck, A. Mukarram, J. Bang, M. Park, H. Choi and S. Lee, *Nanoscale Adv.*, 2026, DOI: 10.1039/D5NA01065A.



This is an Accepted Manuscript, which has been through the Royal Society of Chemistry peer review process and has been accepted for publication.

Accepted Manuscripts are published online shortly after acceptance, before technical editing, formatting and proof reading. Using this free service, authors can make their results available to the community, in citable form, before we publish the edited article. We will replace this Accepted Manuscript with the edited and formatted Advance Article as soon as it is available.

You can find more information about Accepted Manuscripts in the [Information for Authors](#).

Please note that technical editing may introduce minor changes to the text and/or graphics, which may alter content. The journal's standard [Terms & Conditions](#) and the [Ethical guidelines](#) still apply. In no event shall the Royal Society of Chemistry be held responsible for any errors or omissions in this Accepted Manuscript or any consequences arising from the use of any information it contains.

Self-Selective Silver Modification of SiO Anodes: A Conductivity-Boosting Strategy for High-Performance Lithium-Ion Batteries

Asif Raza^{a,b,†}, Panjin Noh^{a,†}, Jaehyuk Yang^{†,a,d}, Mukarram Ali^a, Jae-Yeon Bang^c, Minjoon Park^{d,},
Hae-Young Choi^{a*} and Sang-Min Lee,^{c*}*

^a Next Generation Battery Research Center, Korea Electrotechnology Research Institute, 12, Bulmosan-ro 10 beon-gil, Seongsan-gu, Changwon-si, Gyeongsangnam-do 51543, Republic of Korea

^b Department of Chemistry, University of Ulsan, TechnoSanup-ro 55-gil 12, Nam-gu, Ulsan 44776, Rep. of Korea

^c Graduate Institute of Ferrous & Energy Materials Technology (GIFT), Pohang University of Science and Technology, 77 Cheongam-Ro, Nam-Gu, Pohang, Gyeongbuk, 37673, Republic of Korea

^d Department of Nano Fusion Technology, Pusan National University, Busandaehak-ro 63 beon-gil 2, Geumjeong-gu, Busan 46241, Republic of Korea

† Equal contribution: *Asif Raza^{a,b,†}, Panjin Noh^{a,†}, Jaehyeck Yaong^{a,†}*

*Corresponding authors:

San-Min Lee

^b Graduate Institute of Ferrous & Energy Materials Technology (GIFT), Pohang University of Science and Technology, 77 Cheongam-Ro, Nam-Gu, Pohang, Gyeongbuk, 37673, Republic of Korea



Hae-Young Choi

Next-Generation Battery Research Center, Korea Electrotechnology Research Institute, 12,

Jeongiui-gil, Seongsan-gu, Changwon 51543, Republic of Korea

Tel: +82-55-280-1617

Fax: +82-55-280-1590

Email: ssunzero@keri.re.kr

Minjoon Park

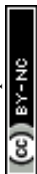
Department of Nano Fusion Technology, Pusan National University

Busandaehak-ro 63 beon-gil 2, Geumjeong-gu, Busan 46241, Republic of Korea

Tel: +82-51-510-3184

Fax: +82-51-514-2358

Email: mjpark@pusan.ac.kr



Abstract

Silicon-based anode materials are highly promising for next-generation lithium-ion batteries (LIBs) due to their superior theoretical capacity. However, their practical implementation is hindered by challenges such as high-volume expansion and low electrical conductivity, leading to rapid capacity degradation. In this study, we synthesized a SiO-Ag composite via a self-selective electroless deposition method to address these limitations. The incorporation of Ag nanoparticles significantly enhanced electrical conductivity and mitigated volume expansion, resulting in improved electrochemical performance. Structural analysis confirmed silver nano clusters distributed on SiO, facilitating efficient lithium-ion transport and charge transfer. Electrochemical evaluations demonstrated an initial Coulombic efficiency of 60.9%, higher than that of pristine SiO (47.8%), along with superior cycling stability over 1000 cycles at 1C with capacity retention of 75% and enhanced rate performance. The reduced charge-transfer resistance, verified through electrochemical impedance spectroscopy, further highlights the beneficial role of Ag modification. These findings provide a viable strategy for optimizing Si-based anodes, paving the way for high-performance and durable LIBs.

Keywords: SiO-Ag, Silicon-based anodes, Lithium-ion batteries, Doping, Cycling stability.



1. Introduction

Lithium-ion batteries (LIBs) are extensively utilized in portable electronics and electric vehicles due to their high energy density, long cycle life, and environmental compatibility¹. Conventional graphite anodes, despite their stability, are limited by a low theoretical specific capacity of 372 mAh g⁻¹, restricting the further improvement of energy density^{2,3}. As the demand for energy storage with higher capacity grows, finding alternative anode materials with superior energy density to replace graphite has become a critical challenge. Silicon (Si), with an ultrahigh theoretical capacity (~4200 mAh g⁻¹) and suitable lithiation potential, is a promising candidate for next-generation LIB anodes⁴⁻⁶. However, its practical application is hampered by significant volume expansion (>300%) during lithiation/delithiation and poor intrinsic electrical conductivity, leading to pulverization, unstable solid electrolyte interphase (SEI) formation, rapid capacity fading, and poor rate performance.⁷⁻¹⁰

Silicon monoxide (SiO) has attracted attention as an alternative to pure silicon owing to its moderate theoretical capacity (~2100 mAh g⁻¹) and relatively better cycling stability¹¹⁻¹⁴. The in-situ formation of Li₄SiO₄ and Li₂O during initial lithiation provides a mechanically robust matrix that buffers volume fluctuations and stabilizes Si nanoclusters^{12,15}. Nevertheless, SiO still suffers from sluggish Li⁺/electron transport and structural instability under high current densities, resulting in limited rate capability and rapid capacity decay during long-term cycling.¹⁶

To overcome these challenges, significant efforts have been made to enhance electrical conductivity and cyclic stability through structural engineering and conductive modifications. Porous architectures, carbon coatings, and metal oxide shells effectively buffer volume changes and shorten Li⁺ diffusion paths, improving cycling performance.¹⁷⁻²⁴. These combinations also



help accommodate the volume changes during cycling, resulting in significantly improved electrochemical performance. Carbon coating is a widely adopted method to improve the electrical conductivity and accommodate volume changes in LIB electrodes^{25–28}. Embedding metals within silicon-based materials has shown promise in providing additional electrical conductivity and mitigating volume expansion, offering a potential pathway to enhance the performance of SiO-based anodes in LIBs^{13,29–31}. For instance, TiO_{2-x} coated porous SiO has demonstrated improved SEI stability and high-rate capability (423.4 mAh g⁻¹ after 500 cycles at 2.0 A g⁻¹) due to oxygen-deficient TiO_{2-x} providing conductive pathways and a robust interfacial layer³². Similarly, embedding conductive metals such as silver (Ag) significantly improves electronic conductivity and mitigates stress during cycling. Ag nanoparticles, when uniformly dispersed within SiO or Si matrices, reduce charge transfer resistance and accelerate Li⁺ diffusion, resulting in superior reversible capacity and rate performance^{30,33}.

Silver-modified SiO composites have proven to be an effective approach, with Ag providing efficient electron conduction that improves the electrical conductivity of the material. For example, Si/Ag@SiO_x and P-SiNPs/Ag@C anodes exhibited remarkable rate performance (1099 mAh g⁻¹ at 2 A g⁻¹) and excellent long-term cycling stability (706 mAh g⁻¹ after 300 cycles at 1 A g⁻¹), attributed to the conductive Ag network and porous structure suppressing SiO pulverization^{33,34}. Building on these advances, this study explores a self-selective electroless (galvanic displacement) deposition strategy that fundamentally differs from conventional metal-decoration approaches. Through a spontaneous redox-driven process conducted under mild conditions, Ag nanoclusters are nucleated and directly anchored onto the SiO surface without the need for external reducing agents, high-energy ball milling, template-assisted synthesis, or multi-step carbonization treatments. Importantly, this deposition process simultaneously induces controlled surface etching,

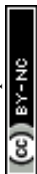


leading to the generation of additional porosity. As a result, a coupled structural evolution occurs: (i) formation of a surface-anchored conductive Ag network and (ii) development of ion-accessible porous pathways. This integrated conductive–porous architecture enhances electronic transport and electrolyte infiltration concurrently, rather than addressing these factors independently. Consequently, the SiO-Ag composite exhibits improved charge-transfer kinetics (lower interfacial resistance and reduced Warburg impedance), enhanced apparent Li^+ diffusion behavior, and stable long-term cycling performance at 1C. Therefore, the significance of this work lies in the process–structure–transport integration enabled by the self-selective electroless route, rather than in the mere addition of Ag.

2. Experimental Section

2.1 Materials Synthesis

All reagents were of analytical grade and used without further purification. Commercial silicon monoxide (SiO , 99.8%, $\sim 10\mu\text{m}$, Alfa Aesar) was employed as the starting material. 2 grams of SiO powder were dispersed in 2 M hydrofluoric acid (HF) and treated for 20 minutes. Subsequently, 10 mM silver nitrate (AgNO_3) solution was introduced into the suspension at room temperature, followed by stirring for certain time to facilitate the deposition of silver on the SiO surface by galvanic displacement reaction. The resulting product was filtered, thoroughly washed with deionized water to remove residual silver precursors, and dried in a vacuum oven at $100\text{ }^\circ\text{C}$ overnight. The obtained material was designated as SiO-Ag.



2.2 Materials Characterization

The crystal structure of the powders was examined using X-ray diffraction (XRD) with a Rigaku instrument (X'pert Philips PMD, Cu K α radiation, $\lambda = 1.5406 \text{ \AA}$). The surface morphology and chemical composition were studied using a field-emission scanning electron microscope (FE-SEM, Hitachi S-4800). Specific surface areas, pore sizes, and pore volumes of the samples were determined using the Brunauer-Emmett-Teller (BET) method with Quantachrome instruments (Autosorb-iQ and Quadrasorb SI). X-ray photoelectron spectroscopy (XPS) spectra were obtained using a ThermoFisher (NEXSA) micro-focused monochromatic X-ray system.

2.3 Electrochemical Measurements

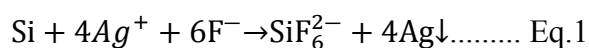
Electrochemical tests were conducted using CR2025-type half-coin cells, which were assembled in an argon-filled glove box with moisture and oxygen levels below 0.1 ppm. Lithium metal foil (500 μm thick) served as both the counter and reference electrode. The working electrodes were prepared by coating a slurry of active material (SiO, SiO-Ag), conductive additive (Super P), and binders (carboxymethyl cellulose (CMC) and polyacrylic acid (PAA)) in a mass ratio of 80:5:7.5:7.5, respectively, on 10 μm thick copper foil. The loading of active material was controlled in the range of 1.1–1.2 mg cm^{-2} for all electrodes. The coated copper foils were dried at 100 $^{\circ}\text{C}$ for 6 hours and subsequently cured under vacuum at 150 $^{\circ}\text{C}$ for 1 hour. The electrodes, with a diameter of 14 mm, were punched, welded onto spacers, and vacuum-dried at 110 $^{\circ}\text{C}$ for 12 hours before assembly. The electrolyte consisted of 1.3 M LiPF $_6$ dissolved in a mixture of ethylene carbonate (EC) and diethyl carbonate (DEC) (3:7 v/v) with 10 wt% fluoroethylene carbonates (FEC) as an additive and a commercial polyethylene (PE) separator of thickness 16 μm



was used. Galvanostatic charge–discharge measurements were conducted using a TOSCAT-3100 battery cycler (TOYO ENGINEERING CORPORATION) within a voltage window of 0.005–1.5 V vs. Li/Li⁺. Pre-cycling was carried out at 0.05 C for one cycle for initial coulombic efficiency and 0.1 C for two cycles within a voltage range of 0.005–2.0 V. Afterward, the cells were cycled at a constant current density of 0.5 C (1.0 C = 1500 mA g⁻¹). Rate capability tests were performed at current densities ranging from 0.1 C to 5.0 C. Cyclic voltammetry (CV) was conducted using a Biologic VSP-200 potentiostat, with a scan rate of 0.05 mV s⁻¹, across a voltage range of 0.005–2.0 V versus Li/Li⁺. The AC impedance measurements were conducted with an amplitude of 5mV over the frequency range of 10mHz to 1 MHz before cycling.

3. Results and Discussion

Figure 1 illustrates the structural and crystalline characteristics of the SiO-Ag composite. In Figure 1a, a schematic illustration depicts the synthesis of the SiO-Ag composite via a self-selective electroless deposition process Eq.1. Commercial SiO (Alpha) powder was dispersed in 2 M hydrofluoric acid (HF) for 20 minutes. Subsequently, 10 mM silver nitrate (AgNO₃) was added, and the suspension was stirred at room temperature for 5 minutes to facilitate silver deposition (optimal sample. See Supporting information, Figure S1). The resulting mixture was filtered, thoroughly rinsed with deionized water to remove residual silver precursors, and dried overnight in a vacuum oven at 100 °C, yielding the SiO–Ag composite.



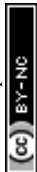
During the galvanic displacement process in the HF-containing solution, partial surface dissolution of SiO occur, potentially forming soluble hexafluorosilicate species ³⁵. In our system, this controlled etching is beneficial, as it generates additional surface porosity that improves electrolyte accessibility and Li⁺ transport. At the same time, Ag nanoclusters nucleate on the SiO surface, forming conductive pathways ^{36,37}. However, excessive etching could increase side reactions; therefore, deposition time was carefully optimized to balance porosity generation and structural stability.

Figure 1b presents the X-ray diffraction (XRD) patterns of the SiO and SiO-Ag samples. The SiO sample exhibits a broad peak, characteristic of an amorphous structure, while the SiO-Ag sample displays additional sharp peaks corresponding to crystalline silver (marked by ●). These results confirm the successful incorporation of crystalline Ag nanoparticles on SiO. Figure 2a-b, shows scanning electron microscopy (SEM) images illustrating the morphological differences between SiO (Figure 2a) and SiO-Ag (Figure 2b) samples. Figure 2a reveal the smooth and compact surface morphology of SiO, with no porosity. In contrast, Figure 2b highlights the significant structural changes in SiO-Ag upon silver incorporation. The SiO-Ag sample exhibits a porous structure with evenly distributed silver particles visible as bright spots account for 16.24 wt% (Figure S2). These Ag-particles are well-embedded on the SiO, suggesting effective integration of silver. The enhanced porosity and uniform distribution of silver contribute to improved surface area and facilitate better ionic and electronic conductivity, which are critical for enhancing the electrochemical performance of the composite material ^{38,39}. This morphological transformation underscores the role of silver in altering the microstructure of SiO to create a more electrochemically favorable architecture.



Table 1 and Figure 2c and d, illustrate the nitrogen adsorption-desorption isotherms and pore size distribution curves for SiO and SiO-Ag, highlighting their textural properties. The SiO sample exhibits a surface area of 0.54 m²/g, a pore volume of 0.0017 m³/g, and an average pore diameter of 4.7 nm. In contrast, the SiO-Ag composite demonstrates a significantly enhanced surface area of 6.16 m²/g, a pore volume of 0.025 m³/g, and an average pore diameter of 13.95 nm. The nitrogen adsorption-desorption isotherms (Figure 2c) show a marked increase in the adsorption volume for SiO-Ag at higher relative pressures, indicating the development of a mesoporous structure upon HF treatment and the incorporation of silver. Similarly, the pore size distribution (Figure 2d) reveals that SiO-Ag possesses a broader pore size range, centered around 13.95 nm, compared to the smaller and less pronounced pores of SiO. These results suggest that the introduction of silver not only enhances the surface area and pore volume but also promotes the formation of larger pores, which are beneficial for improving electrolyte accessibility and ion diffusion during electrochemical processes ⁴⁰.

Figure 3 presents the X-ray photoelectron spectroscopy (XPS) analysis of SiO and SiO-Ag samples, revealing their elemental composition and chemical states. Figure 3a shows the wide-scan XPS spectra of SiO and SiO-Ag highlight the distinct elemental features of the samples. For SiO, peaks corresponding to Si 2p, Si 2s, and O 1s are observed, consistent with the silicon and oxygen composition of the material. In the SiO-Ag spectrum, additional peaks attributed to Ag 3d confirm the successful incorporation of silver into the composite. The presence of C 1s in both spectra likely arises from surface contamination. Figure 3b shows the high-resolution O 1s spectrum of SiO-Ag displays a deconvolution into two distinct peaks located at 532.49 eV and 535.29 eV, corresponding to oxygen species. The peak at 532.49 eV is attributed to Si–O bonds ³⁴, while the higher binding energy peak at 535.29 eV may indicate oxygen associated with surface adsorbed



species or defects ⁴¹ which does not appear in SiO sample (Figure S3a). These features confirm the presence of oxygen-related functionalities within the SiO matrix. Figure 3c shows the high-resolution Si 2p spectrum for SiO-Ag reveals the coexistence of multiple silicon oxidation states. Peaks corresponding to Si⁰, Si⁺, Si²⁺, Si³⁺, and Si⁴⁺ are observed, demonstrating the presence of silicon in varying degrees of oxidation within the composite. SiO (Figure S3b) exhibits similar oxidation states, confirming that the incorporation of Ag into SiO does not alter its composition. This observation aligns with the results obtained from the XRD analysis. Figure 3d shows Ag 3d Spectrum for SiO-Ag sample confirms the presence of metallic silver. The two peaks at 368 eV and 374 eV correspond to Ag 3d_{5/2} and Ag 3d_{3/2}, respectively, with a spin-orbit splitting of 6 eV, indicative of metallic silver. This result confirms that silver is incorporated in its metallic state ⁴², which is critical for enhancing the electrical conductivity of the composite. The XPS analysis confirms the successful integration of silver onto the SiO surface. The coexistence of metallic silver and various silicon states contributes to the improved conductivity and electrochemical performance of the SiO-Ag composite. These results provide valuable insights into the chemical composition and bonding environment, essential for understanding the material's enhanced functionality.

Figure 4 illustrates the electrochemical performance of SiO and SiO-Ag samples using coin cell, showcasing their cyclic voltammetry, charge-discharge profiles, cycling stability, and rate capabilities. Figure 4a, presents the cyclic voltammetry (CV) profiles of SiO and Ag-doped SiO (SiO-Ag) electrodes, recorded in the voltage range of 0.01 to 3.0 V vs Li/Li⁺, providing insights into their electrochemical behavior. Both electrodes exhibit a broad cathodic peak below 0.5 V, corresponding to the lithiation of SiO to form Li_xSi and the decomposition of electrolyte, leading to SEI (solid electrolyte interphase) formation. The anodic peaks observed around 0.3-0.6 V



represent the delithiation process of Li_xSi . Notably, the SiO-Ag electrode exhibits sharper and more pronounced current responses compared to the pristine SiO, indicating improved electrochemical reversibility and faster redox kinetics. The higher peak intensity and steeper slope of the redox peaks in the SiO-Ag sample suggest enhanced conductivity, likely attributed to the introduction of highly conductive silver nanoparticles. This improvement facilitates more efficient charge transfer during the electrochemical reaction, consistent with the enhanced cycling and rate performance observed in earlier galvanostatic tests. Thus, Ag doping significantly boosts the electrochemical activity of the SiO-based anode material. In Figure 4b, the charge and discharge capacities are shown to be significantly higher for SiO-Ag (2050.52 mA h g⁻¹ and 1249.17 mA h g⁻¹, respectively), compared to SiO (1868.58 mA h g⁻¹ and 892.89 mA h g⁻¹), resulting in initial Coulombic efficiencies (ICE) of 47.8% for SiO and 60.9% for SiO-Ag. Figure 4c demonstrates the long-term cycling stability, where SiO-Ag exhibits superior capacity retention of 78% after 300 cycles, compared to 51% for SiO at 0.5C (1C = 1500 mA g⁻¹). The first decay in the capacities of samples is due to the volume expansion effect of silicon particles in the cycling process. The repetitive volume changes could fracture the SEI layers and result in a more extensive exposure of Si active sites during the lithiation process. The fresh active site could provide more sites to store charge, thereby increasing capacity after few initial cycles^{12,13}. It should be noted that the specific capacities reported in this study are normalized to the total mass of active material, including the Ag component in the SiO-Ag composite (≈16 wt%). Although Ag does not significantly contribute to Li storage within the investigated voltage range, its incorporation enhances electronic conductivity and charge-transfer kinetics. To further confirm the effect of Ag on SiO, Ag was selectively removed using a solution containing 1 mole of HF and 0.06 moles of H₂O₂. The electrochemical performance of the samples before and after Ag removal was evaluated and is



presented in Figure S4(a). While Pitch has been utilized as a carbon source for coating SiO anodes, our current work identifies limitations in its suitability for SiO materials (Figure S4b). Carbon coatings serve a similar purpose by providing a conductive network that mitigates the effects of SiO's volume expansion during cycling. However, as previously discussed, the application of carbon coatings on SiO anodes must be carefully optimized to balance conductivity enhancement with potential drawbacks such as reduced capacity and increased first-cycle irreversible capacity⁴³. Results demonstrate that Ag doping significantly improves the cycling stability. The rate performance, as depicted in Figure 4d, reveals that SiO-Ag outperforms SiO across various current densities, with specific capacities of 1105, 775, 553, 450, and 312 mA h g⁻¹ at 0.2C, 0.5C, 1.0C, 3.0C, and 5.0C, respectively, and recovers to 877 mA h g⁻¹ when returned to 0.2C which is marginally lower than the initial value, possibly attributed to partial material degradation induced by high-rate cycling. In comparison, SiO shows lower capacities of 933, 660, 381, 168, and 12 mA h g⁻¹ at the same rates, with only 286 mA h g⁻¹ upon recovery. Figure 4e, illustrates the cycling performance of the anodes at a high current density of 1.0 C. After 1000 cycles, the SiO-Ag anode retains a reversible capacity of 386 mA h g⁻¹, corresponding to approximately 75% capacity retention for 1C compared at 3rd cycle after 2 formation cycles. In contrast, the SiO anode shows significantly lower performance, with only 10% capacity retention over the same period. Comparative studies of the SiO₂ carbon composites are listed in a separate table in supplementary information (Table. S1). Furthermore, Figure 5a and b, displays cross-sectional SEM images of the SiO-Ag electrode (a) before and (b) after long-term electrochemical cycling. Initially, the electrode thickness is approximately 11.5 μm, with a relatively compact microstructure. After cycling, the electrode expands to about 15.1 μm, indicating significant structural changes. This increase in thickness and the more porous morphology suggests volume expansion and mechanical



stress induced by repeated lithiation/delithiation processes. Despite the expansion, the electrode maintains good structural integrity and preserving electrode stability during prolonged cycling. These results highlight the enhanced electrochemical performance of SiO-Ag, attributed to the improved conductivity and structural stability imparted by pore generation Ag doping⁴⁰.

Figure 5c presents the Nyquist plot with fitting, illustrating the effect of Ag incorporation on the electrochemical impedance of SiO. The plot depicts the imaginary impedance (Z'') on the y-axis versus the real impedance (Z') on the x-axis. The semicircle appearing at high-to-mid frequencies represents the surface (R_s) and film resistance (R_f), while the semicircle in the low-frequency region corresponds to the charge-transfer resistance (R_{ct}) at the electrode-electrolyte interface^{44,45}. The low-frequency straight-line segment indicates Warburg impedance, which is related to ion diffusion within the electrolyte or electrode material. Compared to SiO, the SiO-Ag composite exhibits lower R_s and R_f and a smaller semicircle, signifying reduced surface and charge-transfer resistance. Additionally, the steeper slope in the Warburg region suggests enhanced ionic diffusion. The incorporation of Ag improves the composite's electrical conductivity, promoting more efficient charge transfer at the electrode-electrolyte interface. This improvement in ionic diffusion may be attributed to a more interconnected network structure or reduced particle agglomeration facilitated by Ag. This enhancement is further supported by the calculated lithium-ion diffusion coefficients, which are significantly improved for SiO-Ag ($2.2 \times 10^{-7} \text{ cm}^2 \text{ s}^{-1}$) compared to pristine SiO ($2.5 \times 10^{-9} \text{ cm}^2 \text{ s}^{-1}$) Table S2 and Figure S5. This two-orders-of-magnitude increase in D_{Li^+} confirms that Ag facilitates faster ion transport, likely due to a more conductive and interconnected network or reduced particle agglomeration. Overall, the SiO-Ag composite demonstrates superior electrochemical performance compared to pure SiO, primarily due to the synergistic effect of Ag, which enhances charge-transfer kinetics and ion transport.



4. Conclusion

In this study, we successfully synthesized a SiO-Ag composite using a self-selective electroless deposition method, demonstrating its potential as an anode material for lithium-ion batteries. The incorporation of Ag significantly enhanced electrical conductivity and mitigated volume expansion, resulting in improved electrochemical performance. Structural and morphological analyses confirmed the formation of a porous SiO with well-dispersed Ag nanoparticles, promoting better lithium-ion diffusion and charge transfer. Electrochemical tests revealed a superior initial Coulombic efficiency of 60.9%, compared to 47.8% for pristine SiO at 0.1C and better capacity retention of 75% at 1C for SiO-Ag composite. The SiO-Ag composite also exhibited enhanced cycling stability, maintaining a higher capacity retention of 75% for 1 after 1000 prolonged cycling. Additionally, rate capability tests confirmed its ability to sustain high specific capacities at elevated current densities. These findings provide valuable insights into the development of high-performance anode materials. Future studies may focus on further optimizing Ag content and exploring scalable fabrication techniques for commercial applications based on full-cell integration, involving pre-lithiation and electrolyte optimization to address lithium inventory loss.

5. Acknowledgement



This research was supported by the National Research Council of Science & Technology(NST) grant by the Korea government (MSIT) (No. GTL24011-000), and was supported by a 'Regional innovation mega project' program through the Korea Innovation Foundation funded by Ministry of Science and ICT (Project Number: 2023-DD-UP-0332) and by Korea Institute for Advancement of Technology (KIAT) grant funded by the Korea Government (MOTIE) (RS-2024-00419413, HRD Program for Industrial Innovation)



References:

- 1 M. Armand, P. Axmann, D. Bresser, M. Copley, K. Edström, C. Ekberg, D. Guyomard, B. Lestriez, P. Novák and M. Petranikova, *J. Power Sources*, 2020, **479**, 228708.
- 2 T. Chen, J. Wu, Q. Zhang and X. Su, *J. Power Sources*, 2017, **363**, 126–144.
- 3 S. Wu, Y. Han, K. Wen, Z. Wei, D. Chen, W. Lv, T. Lei, J. Xiong, M. Gu and W. He, *Compos. Part B Eng.*, 2019, **161**, 369–375.
- 4 H. Zhao, J. Li, Q. Zhao, X. Huang, S. Jia, J. Ma and Y. Ren, *Electrochem. Energy Rev.*, 2024, **7**, 11.
- 5 M. K. Majeed, R. Iqbal, A. Hussain, M. U. Majeed, M. Z. Ashfaq, M. Ahmad, S. Rauf and A. Saleem, *Crit. Rev. Solid State Mater. Sci.*, 2024, **49**, 221–253.
- 6 G. F. I. Toki, M. K. Hossain, W. U. Rehman, R. Z. A. Manj, L. Wang and J. Yang, *Ind. Chem. Mater.*
- 7 M. W. Verbrugge, D. R. Baker, X. Xiao, Q. Zhang and Y.-T. Cheng, *J. Phys. Chem. C*, 2015, **119**, 5341–5349.
- 8 J.-S. Bridel, T. Azais, M. Morcrette, J.-M. Tarascon and D. Larcher, *Chem. Mater.*, 2010, **22**, 1229–1241.
- 9 T. Yoon, C. C. Nguyen, D. M. Seo and B. L. Lucht, *J. Electrochem. Soc.*, 2015, **162**, A2325.
- 10 S. Guo, H. Li, Y. Li, Y. Han, K. Chen, G. Xu, Y. Zhu and X. Hu, *Adv. Energy Mater.*, 2018, **8**, 1800434.
- 11 J. Wang, H. Zhao, J. He, C. Wang and J. Wang, *J. Power Sources*, 2011, **196**, 4811–4815.



- 12 A. Raza, S. Y. Kim, J.-H. Choi, J.-S. Kim, M.-S. Park and S.-M. Lee, *Int. J. Energy Res.*, DOI: <https://doi.org/10.1002/er.8443>.
- 13 A. Raza, J. Y. Jung, C.-H. Lee, B. G. Kim, J.-H. Choi, M.-S. Park and S.-M. Lee, *ACS Appl. Mater. Interfaces*, 2021, **13**, 7161–7170.
- 14 Y. Hwa, C.-M. Park and H.-J. Sohn, *J. Power Sources*, 2013, **222**, 129–134.
- 15 X. Meng, H. Huo, Z. Cui, X. Guo and S. Dong, *Electrochim. Acta*, 2018, **283**, 183–189.
- 16 A. Casimir, H. Zhang, O. Ogoke, J. C. Amine, J. Lu and G. Wu, *Nano Energy*, 2016, **27**, 359–376.
- 17 A. Reyes Jiménez, R. Klöpsch, R. Wagner, U. C. Rodehorst, M. Kolek, R. Nölle, M. Winter and T. Placke, *ACS Nano*, 2017, **11**, 4731–4744.
- 18 H. Wu, G. Chan, J. W. Choi, I. Ryu, Y. Yao, M. T. McDowell, S. W. Lee, A. Jackson, Y. Yang and L. Hu, *Nat. Nanotechnol.*, 2012, **7**, 310.
- 19 N. Liu, J. Liu, D. Jia, Y. Huang, J. Luo, X. Mamat, Y. Yu, Y. Dong and G. Hu, *Energy Storage Mater.*, 2019, **18**, 165–173.
- 20 Y. Han, J. Zhou, T. Li, Z. Yi, N. Lin and Y. Qian, *Nano Res.*, 2018, **11**, 6294–6303.
- 21 C. Xu, Q. Hao and D. Zhao, *Nano Res.*, 2016, **9**, 908–916.
- 22 F. Guo, P. Chen, T. Kang, Y. L. Wang, C. H. Liu, Y. Shen, W. Lu and L. Chen, *Acta Phys.-Chim. Sin.*, 2019, **35**, 1365–1371.
- 23 X. Zhang, D. Kong, X. Li and L. Zhi, *Adv. Funct. Mater.*, 2019, **29**, 1806061.
- 24 Y. Tian, Y. An and J. Feng, *ACS Appl. Mater. Interfaces*, 2019, **11**, 10004–10011.



- 25 X. Guo, Y.-Z. Zhang, F. Zhang, Q. Li, D. H. Anjum, H. Liang, Y. Liu, C. Liu, H. N. Alshareef and H. Pang, *J. Mater. Chem. A*, 2019, **7**, 15969–15974.
- 26 P. Lv, H. Zhao, Z. Li, C. Gao and Y. Zhang, *Solid State Ionics*, 2019, **340**, 115024.
- 27 K. W. Kim, H. Park, J. G. Lee, J. Kim, Y.-U. Kim, J. H. Ryu, J. J. Kim and S. M. Oh, *Electrochim. Acta*, 2013, **103**, 226–230.
- 28 T. Meng, B. Li, C. Liu, Q. Wang, D. Shu, S. Ou, M. S. J. T. Balogun, H. Su and Y. Tong, *Energy Storage Mater.*, 2022, **46**, 344–351.
- 29 A. Raza, J.-Y. Bang, H.-Y. Kim, J.-H. Choi, H.-Y. Choi and S.-M. Lee, *Sci. Technol. Adv. Mater.*, 2025, **26**, 2485868.
- 30 G. Xu, C. Jin, Y. Lan, L. Liu, K. Kong, X. Yang, Z. Yue, X. Li, F. Sun and H. Huang, *Mater. Lett.*, 2018, **233**, 228–232.
- 31 J. Zhang, J. Zhang, T. Bao, X. Xie and B. Xia, *J. Power Sources*, 2017, **348**, 16–20.
- 32 Y. Xu, Y. Li, Y. Qian, S. Sun, N. Lin and Y. Qian, *Inorg. Chem. Front.*, 2023, **10**, 1176–1186.
- 33 Y. Li, G. Chen, W. Liu, L. Huang and X. Luo, *Waste Manag.*, 2023, **156**, 22–32.
- 34 P. Ouyang, C. Jin, G. Xu, X. Yang, K. Kong, B. Liu, J. Dan, J. Chen, Z. Yue and X. Li, *Ceram. Int.*, 2021, **47**, 1086–1094.
- 35 D. Kim, J. Han, O.-S. Jung and Y.-A. Lee, *RSC Adv.*, 2022, **12**, 25118–25122.
- 36 Y. Liu, G. Ji, J. Wang, X. Liang, Z. Zuo and Y. Shi, *Nanoscale Res. Lett.*, 2012, **7**, 663.
- 37 B. M. Bang, J.-I. Lee, H. Kim, J. Cho and S. Park, *Adv. Energy Mater.*



- 38 W. An, B. Gao, S. Mei, B. Xiang, J. Fu, L. Wang, Q. Zhang, P. K. Chu and K. Huo, *Nat. Commun.*, 2019, **10**, 1447.
- 39 J. Wang, L. Liao, H. R. Lee, F. Shi, W. Huang, J. Zhao, A. Pei, J. Tang, X. Zheng and W. Chen, *Nano Energy*, 2019, **61**, 404–410.
- 40 F. Xi, Z. Zhang, X. Wan, S. Li, W. Ma, X. Chen, R. Chen, B. Luo and L. Wang, *ACS Appl. Mater. Interfaces*, 2020, **12**, 49080–49089.
- 41 Y. Zhong, X. Qiu, J. Gao and Z. Guo, *Isij Int.*, 2019, **59**, 1098–1104.
- 42 G. Zou, Z. Zhang, J. Guo, B. Liu, Q. Zhang, C. Fernandez and Q. Peng, *ACS Appl. Mater. Interfaces*, 2016, **8**, 22280–22286.
- 43 A. R. Iarchuk, V. A. Nikitina, E. A. Karpushkin, V. G. Sergeyev, E. V Antipov, K. J. Stevenson and A. M. Abakumov, *ChemElectroChem*, 2019, **6**, 5090–5100.
- 44 X. Lu, N. Zhang, M. Jahn, W. Pfleging and H. J. Seifert, *Appl. Sci.*, 2019, **9**, 3671.
- 45 A. Raza, F. Ghani, J. Lim, I. W. Nah and H.-S. Kim, *Microporous Mesoporous Mater.*, 2021, **314**, 110853.



Data Availability Statement

All data supporting the findings of this study, including XRD, XPS, SEM, BET, and electrochemical measurement results, are provided in the Supplementary Information of this article. Additional raw data are available from the corresponding author upon reasonable request.

